

Sputtering in oblique C-type shocks

S. Van Loo,^{1*}, I. Ashmore,², P. Caselli², S. A. E. G. Falle³ and T. W. Hartquist²

¹ *Harvard-Smithsonian Center for Astrophysics, 60 Garden St., Cambridge, Massachusetts 02138, USA*

² *School of Physics and Astronomy, University of Leeds, Leeds LS2 9JT, UK*

³ *Department of Applied Mathematics, University of Leeds, Leeds LS2 9JT, UK*

Accepted -. Received -; in original form -

ABSTRACT

We present the first results for the sputtering of grain mantles and cores obtained with self-consistent multifluid hydromagnetic models of C-type shocks propagating through dusty media. The threshold shock speed for mantle sputtering is about 10 km s^{-1} and is independent of density. The mantles are completely vapourised in shocks with speeds of $20\text{--}25 \text{ km s}^{-1}$. At such shock speeds core sputtering commences and gas-phase SiO forms. Core destruction is not total in any C-type shock because grains are not completely destroyed in shocks with speeds near the minimum speeds at which J-type shocks appear. Due to the density-dependence of the critical shock speed for this transition, higher gas-phase SiO fractional abundances are produced behind shocks propagating in lower density gas. For shock speeds near the threshold speeds for both core and mantle sputtering, sputtering is much greater for shock velocities at smaller angles relative to the upstream magnetic field. At higher shock speeds, the angular variation is still present but less pronounced.

Key words: MHD – shockwaves – ISM: dust – ISM: jets and outflows.

1 INTRODUCTION

A number of computational studies of sputtering in self-consistent models of perpendicular C-type hydromagnetic shocks in dusty, dark regions have been performed (e. g. Flower & Pineau des Forêts 1995; Schilke et al. 1997; May et al. 2000; Gusdorf et al. 2008b; Guillet et al. 2011). However, the only numerical investigation of sputtering in oblique C-type shocks in such regions is not based on self-consistent shock models (Caselli et al. 1997).

Pilipp & Hartquist (1994) attempted to construct a self-consistent, four fluid model of an oblique C-type shock in which dust grains are described as a charged fluid, as they are in the perpendicular C-type shock models of Pilipp et al. (1990). However, the integrations performed by Pilipp & Hartquist (1994) failed to yield solutions corresponding to steady fast-mode shocks. Wardle (1998) pointed out that the failure is due to the saddle-point nature of the downstream state of a fast-mode dusty shock. Falle (2003) developed a numerical scheme for solving the time-dependent multifluid hydromagnetic equations that enables the construction of steady fast-mode solutions even when local equilibrium does not obtain. Van Loo et al. (2009) have used the scheme along with non-equilibrium chemistry and treatments of grain charge and heating and radiative losses to investigate the evolution of oblique C-type shocks propagating into media with constant upstream properties. Ashmore et al. (2010) extended the applications to oblique C-type

shocks propagating through media with varying upstream properties.

Here we use models like those of Van Loo et al. (2009) to study sputtering in oblique C-type shocks in dusty, dark molecular regions. Section 2 contains descriptions of the assumptions, the physical processes included, the chemical network, the evaluation of the sputtering rates and upstream boundary conditions. Results are presented in Section 3, and Section 4 contains a discussion of the results and conclusions.

2 THE MODEL

The model includes neutral, ion, electron and two grain fluids. Flow variables depend on only the spatial coordinate x and time t . The upstream magnetic field has components in the x and y directions, and the shock propagates in the x direction. Equations 1 – 8 of Van Loo et al. (2009) are solved with the scheme of Falle (2003). The inertia of the charged fluids, including the grain fluids, is neglected in this approach, so that their dynamics is solely determined by the balance between the Lorentz force and collision forces with neutral particles. Additionally, the grain fluids are assumed to have zero pressure. The average charge on a grain is determined by the condition that the magnitude of the current of ions onto a grain equals the magnitude of the current of electrons onto a grain; Eqs. 10 and 11 of Havnes et al. (1987, see also Appendix A) are used to calculate these currents. The numerical method of Falle (2003) provides a rigorous means to model steady shock structures and, as discussed by (Van Loo et al. 2009) and Ashmore et al.

* E-mail: svanloo@cfa.harvard.edu

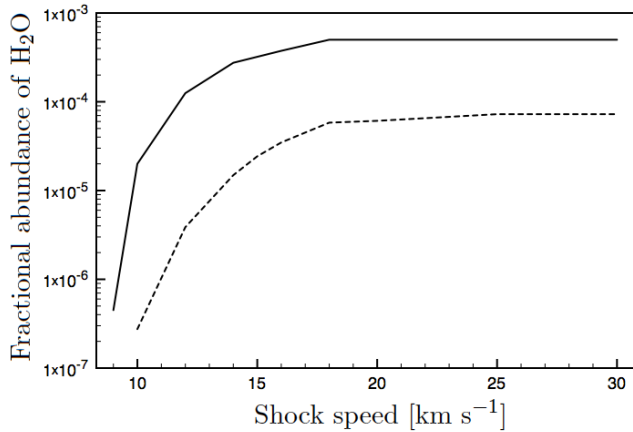


Figure 1. The fractional abundance of H_2O produced by gas-phase chemistry (solid) and mantle sputtering (dashed) as function of the shock speed for $n_{\text{H}_0} = 10^6 \text{ cm}^{-3}$.

(2010), reproduces the results of, among others, Draine et al. (1983), Pilipp & Hartquist (1994), Chapman & Wardle (2006) and Guillet, Pineau des Forêts, & Jones (2007). Furthermore, although it neglects grain inertia, the method can accurately model neutral subshock structures (Falle 2003; Ashmore et al. 2010).

The evolution of the number density, $n(X)$, of chemical species X is governed by a rate equation of the form:

$$\frac{\partial n(X)}{\partial t} + \frac{\partial n(X)u_s}{\partial x} = s(X), \quad (1)$$

u_s is the x component of the ion or neutral velocity depending on whether X is an ion or a neutral. $s(X)$ is the net rate of formation or destruction of species X per unit volume per unit time due to the gas phase reactions and grain surface recombinations listed in Table 1 and the return of material to the gas phase due to sputtering. Though no reactions involving SiO are shown in Table 1, atomic Si returned to the gas phase due to sputtering is assumed to be converted to SiO immediately.

The model includes the radiative losses due to O, CO, H_2 and H_2O , which are calculated for the abundances of O and H_2O given by the integration of the chemical rate equations and the assumed constant fractional abundances of CO and H_2 . Given those abundances, the cooling rates are evaluated as they were by Van Loo et al. (2009). They adopted the treatments of Draine et al. (1983) for the cooling of electrons and for OI emission, used data from Hartquist et al. (1980) for the cooling of neutrals by H_2 and implemented the treatment of CO cooling due to Hollenbach & McKee (1979) and that of H_2O cooling developed by Neufeld & Melnick (1987).

Sputtering due to H_2 , CO, O, Mg, H_2O and SiO projectiles is included. As mentioned above, the return of material to the gas phase due to sputtering contributes to the source terms in the rate equations governing the gas phase chemistry; these contributions to the source terms are particularly important for the model gas phase abundances of Mg, H_2O and SiO . A grain consists of a refractory core made of olivine (MgFeSiO_4) and a mantle of water ice. A core remains intact until all of the ice has been sputtered. The sputtering rates are calculated as they were by Jiménez-Serra et al. (2008), who used Eq. 27 of Draine & Salpeter (1979) for the sputtering rate. For all projectiles, they used Eq. 31 of Draine & Salpeter (1979) to obtain the sputtering yields of ice at normal incidence. They used the same equation to obtain the corresponding yield

for core material colliding with H_2 . However, for projectiles other than H_2 , they employed the results of May et al. (2000) for the sputtering yields of core material at normal incidence. Following Draine & Salpeter (1979), Jiménez-Serra et al. (2008) took the angle averaged value of a yield to be twice the value of the normal incidence yield.

The upstream magnetic field strength is $B_0 = 1\mu\text{G}(n_{\text{H}_0}/1 \text{ cm}^{-3})^{1/2}$, where n_{H_0} is the upstream value of n_{H} , the number density of hydrogen nuclei. A shock propagates with a speed v_s at an angle θ with respect to the upstream magnetic field (for an oblique shock, $0^\circ \leq \theta \leq 90^\circ$). The grains have radii of $0.4 \mu\text{m}$ and $0.04 \mu\text{m}$ and masses of $8.03 \times 10^{-13} \text{ g}$ and $8.03 \times 10^{-16} \text{ g}$. In the upstream region, one percent of the mass is contained in grains with the number density of smaller grains 316 times that of the larger grains (i.e. the grains follow the grain-size distribution of Mathis et al. (1977)). As all the grains are silicate-based in our model, the fractional abundance of Si, i.e. 5.8×10^{-5} , is somewhat higher than the cosmic value of 3.37×10^{-5} (Anders & Grevesse 1989). The fractional abundance of CO to hydrogen nuclei has a constant value of 5×10^{-5} ahead, throughout and behind the shock, and the upstream gas phase fractional abundances of O, Mg, H_2O and SiO are 4.25×10^{-4} , 10^{-7} , 0 and 0, respectively. Note that, including the fractional abundance of CO and of olivine, the total abundance of O in our model exceeds the cosmic abundance of O by less than a factor of two (the latest measured value being 3.2×10^{-4} (Meyer, Jura, & Cardelli 1998) although Snow & Witt (1996) give 4.6×10^{-4}). The initial fractional ionisation is calculated as it was by Van Loo et al. (2009); HCO^+ and Mg^+ are initially the only ions, but the chemistry leads to the production of significant fractional abundances of H_3^+ and H_3O^+ before heating by the shock occurs. Although upstream of a shock there is no water in the gas phase, the upstream fractional abundance of water ice molecules on the grains is 7.25×10^{-5} (cf. Whittet & Duley 1991); the upstream value of the ratio of the total mass of ice on small grains to the total mass of ice on big grains is taken to be 3.16.

We followed Van Loo et al. (2009) by assuming that the initial flow corresponds to that of a J-type shock. The presented results are for the steady flows yielded by time integrations.

3 RESULTS

We focus on the abundances of H_2O and SiO as mantle and core sputtering releases these molecules into the gas phase. However, water is also produced by shock chemistry. To quantify the contributions of both processes we discuss the chemistry first and then grain sputtering.

3.1 Shock chemistry

The specified initial relative abundances are not in steady state chemical equilibrium. The upstream gas phase ion abundances initially evolve on a timescale short compared to the flow time through the shock and then evolve further as the abundances of other key species (e. g. H_2O) vary. H_3O^+ and HCO^+ are the most common molecular ions, but the Mg^+ fractional abundance is about an order of magnitude greater than the total fractional abundance of molecular ions. The ratio of the total atomic ion abundance to the total molecular abundance depends on the assumed elemental abundance of metals.

Table 1. The chemical network. The column titled "Num." lists the reaction number, that labelled "Reaction" gives the reaction partners and products for each, that designated "Rate or Rate Coefficient" lists the adopted rates and rate coefficients and that labelled "Ref." gives the source of each coefficient: Source 1 is Pilipp et al. (1990), 2 is the UDFA database described by Woodall et al. (2007), 3 is Guillet et al. (2009) and 4 indicates that the value is calculated with a routine in the code.

Num.	Reaction	Rate (s^{-1}) or Rate Coefficient ($cm^3 s^{-1}$)	Ref.
1 ^a	$H_2 + CR \rightarrow H_3^+ + e + CR$	3×10^{-17}	1
2	$H_3^+ + CO \rightarrow HCO^+ + H_2$	1.7×10^{-9}	1, 2, 3
3	$H_3^+ + H_2O \rightarrow H_3O^+ + H_2$	5.9×10^{-9}	2, 3
4	$H_3^+ + \text{grain}^- \rightarrow H_2 + H + \text{grain}$	$(\Gamma_{ig} + \Gamma_{is}) n(H_3^+)/n_i$	4
5	$H_3^+ + O \rightarrow H_3O^+$	8.4×10^{-10}	2, 3
6	$HCO^+ + e \rightarrow H + CO$	$2.76 \times 10^{-7} (T_e/300)^{-0.64}$	3
7	$HCO^+ + Mg \rightarrow H + CO + Mg^+$	2.9×10^{-9}	2
8	$HCO^+ + H_2O \rightarrow H_3O^+ + CO$	2.5×10^{-9}	2, 3
9	$HCO^+ + \text{grain}^- \rightarrow H + CO + \text{grain}$	$(\Gamma_{ig} + \Gamma_{is}) n(HCO^+)/n_i$	4
10	$Mg^+ + e \rightarrow Mg + h\nu$	$2.8 \times 10^{-12} (T_e/300)^{-0.86}$	1, 2
11	$Mg^+ + \text{grain}^- \rightarrow Mg + \text{grain}$	$(\Gamma_{ig} + \Gamma_{is}) n(Mg^+)/n_i$	4
12 ^b	$Mg^+ + H_2 \rightarrow MgH^+ + H$	$3.0 \times 10^{-10} \exp(-27854/T_{\text{eff}})$	1
13	$MgH^+ + e \rightarrow Mg + H$	$1.1 \times 10^{-7} (T_e/300)^{-0.5}$	1
14	$MgH^+ + \text{grain}^- \rightarrow Mg + H + \text{grain}$	$(\Gamma_{ig} + \Gamma_{is}) n(MgH^+)/n_i$	4
15 ^c	$H_3O^+ + e \rightarrow H_2O + H$	$3.29 \times 10^{-7} (T_e/300)^{-0.5}$	2, 3
16	$H_3O^+ + Mg \rightarrow H_2O + Mg^+ + H$	1.8×10^{-9}	1
17	$H_3O^+ + \text{grain}^- \rightarrow H_2O + H + \text{grain}$	$(\Gamma_{ig} + \Gamma_{is}) n(H_3O^+)/n_i$	4
18 ^d	$O + H_2 \rightarrow H_2O$	$3.14 \times 10^{-13} (T_n/300)^{2.7} \exp(-3150/T_n)$	2, 3

^a Reaction 1 is an amalgamation of two reactions: $H_2 + CR \rightarrow H_2^+ + e + CR$ and $H_2^+ + H_2 \rightarrow H_3^+ + H$ where CR denotes a cosmic ray. The adopted coefficient is that of the first reaction since the proton transfer reaction occurs sufficiently rapidly.

^b T_{eff} in the rate coefficient of Reaction 12 defines a weighted kinetic temperature at the ion-neutral drift speed and is given by Eq. 43 of Flower et al. (1985).

^c Reaction 15 is an amalgamation of:

$H_3O^+ + e \rightarrow OH + H_2$ ($6.02 \times 10^{-8} (T_e/300)^{-0.5}$),
 $H_3O^+ + e \rightarrow OH + H + H$ ($2.58 \times 10^{-7} (T_e/300)^{-0.5}$) and
 $H_3O^+ + e \rightarrow H_2O + H$ ($1.08 \times 10^{-8} (T_e/300)^{-0.5}$).

OH is not treated as a separate species, because the OH produced by the first two reactions quickly reacts with H_2 to yield H_2O (see ^d).

^d Reaction 18 is also an amalgamation of two reactions: $O + H_2 \rightarrow OH + H$ and $OH + H_2 \rightarrow H_2O + H$. The coefficient adopted is that of the first (slower) of the two.

Table 2. Fraction of mantle that is sputtered and gas phase water fractional abundance enhancement due to sputtering. Results are given for large and small grains and for both combined. Although some small grain sputtering does occur in the 9 km s^{-1} , $n_{H0} = 10^6 \text{ cm}^{-3}$ case, the fraction of ice removed was $< 10^{-4}$.

Shock Speed (km s^{-1})	n_{H0} (cm^{-3})	Large grains		Small grains		Large & Small grains	
		Fraction of ice removed	Contribution to downstream H_2O	Fraction of ice removed	Contribution to downstream H_2O	Fraction of ice removed	Contribution to downstream H_2O
10	1.00(4)	1.20(-3)	3.09(-8)	3.80(-3)	2.09(-7)	3.31(-3)	2.40(-7)
12	1.00(4)	4.00(-2)	1.04(-6)	5.50(-2)	3.03(-6)	5.61(-2)	4.07(-6)
14	1.00(4)	1.75(-1)	3.05(-6)	2.00(-1)	1.10(-5)	1.94(-1)	1.41(-5)
16	1.00(4)	4.50(-1)	7.83(-6)	4.80(-1)	2.64(-5)	4.72(-1)	3.42(-5)
20	1.00(4)	1.00	1.74(-5)	1.00	5.51(-5)	1.00	7.25(-5)
8	1.00(6)	0.00	-	0.00	-	0.0	-
9	1.00(6)	0.00	-	$< 1.00(-4)$	≈ 0.00	$< 1.00(-4)$	≈ 0.00
10	1.00(6)	0.00	-	5.00(-3)	2.75(-7)	3.79(-3)	2.75(-7)
12	1.00(6)	2.50(-3)	4.36(-8)	6.95(-2)	3.83(-6)	5.34(-2)	3.87(-6)
14	1.00(6)	2.50(-2)	4.36(-7)	2.63(-1)	1.45(-5)	2.06(-1)	1.49(-5)
15	1.00(6)	5.00(-2)	8.71(-7)	4.25(-1)	2.34(-5)	3.35(-1)	2.43(-5)
16	1.00(6)	7.78(-2)	1.36(-6)	6.07(-1)	3.34(-5)	4.79(-1)	3.48(-5)
18	1.00(6)	1.8(-1)	3.14(-6)	1.00	5.51(-5)	8.03(-1)	5.82(-5)
20	1.00(6)	3.4(-1)	5.93(-6)	1.00	5.51(-5)	8.42(-1)	6.10(-5)
25	1.00(6)	1.00	1.74(-5)	1.00	5.51(-5)	1.00	7.25(-5)

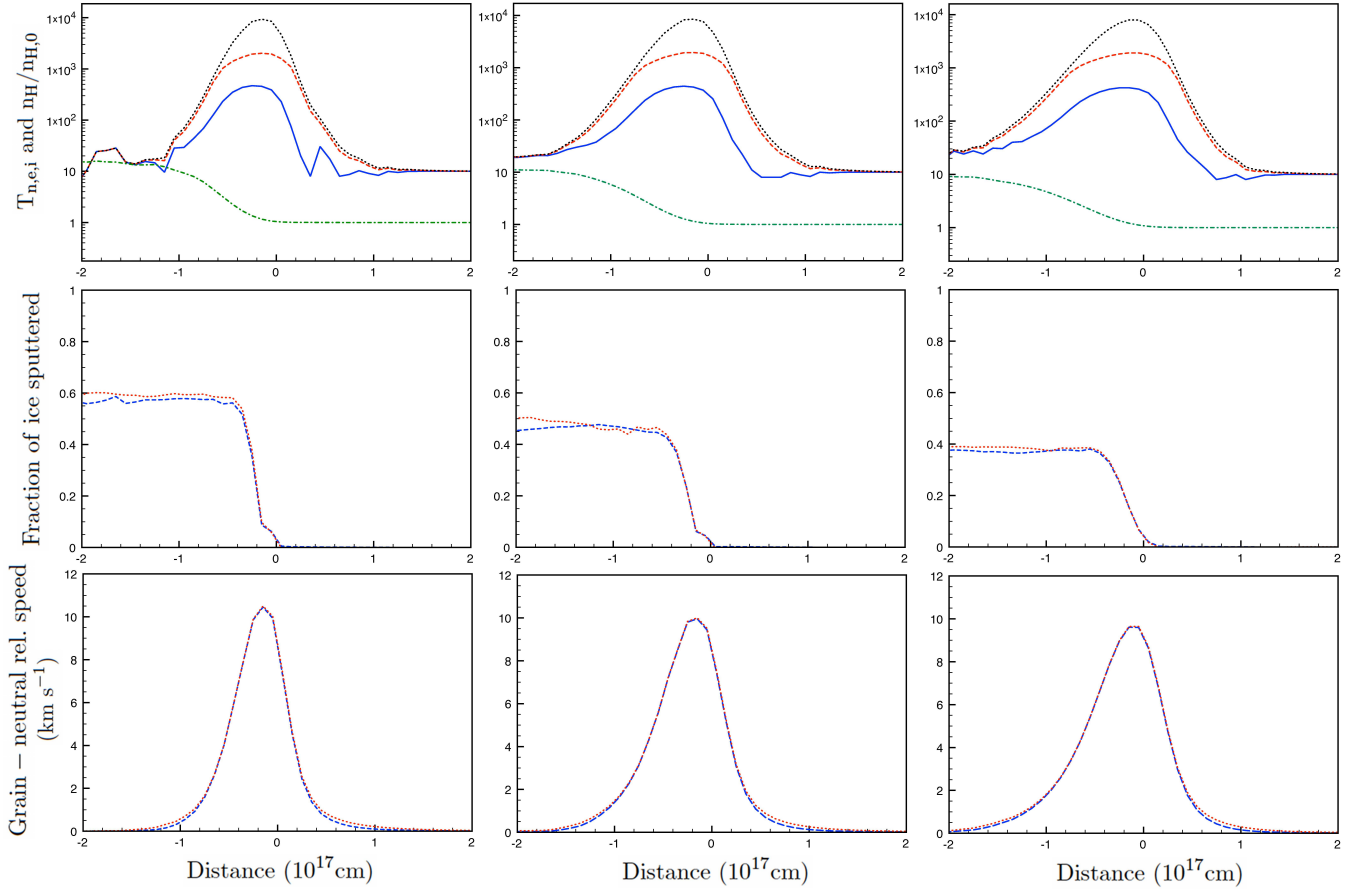


Figure 2. Fraction of ice ejected from grain mantles for a shock speed of 16 km s^{-1} , $n_{\text{H}_2\text{O}} = 10^4 \text{ cm}^{-3}$ and θ of 30° (left), 45° (middle) and 60° (right). The top row gives the ion (black, dotted), electron (red, dashed) and neutral (blue, solid) temperatures, as well as the neutral density normalised to its upstream value (green, dash-dotted). The middle row shows the fraction of ice ejected from large (blue, dashed) and small (red, dotted) grains. The bottom row displays the speed of small (red, dotted) and large (blue, dashed) grains relative to neutrals in km s^{-1} .

The assumed upstream water fractional abundance is about three orders of magnitude below the water fractional abundances obtained with standard ion-molecule chemical models, i.e. $\sim 10^{-6}$ (e.g. Millar et al. 1997; Neufeld et al. 1995). However, the upstream value is close to the water abundances of $\sim 10^{-8}$ inferred for quiescent molecular gas towards Orion, M17 and other sources by Bergin et al. (2000). Recent Herschel observations of ortho- H_2O in a dark cloud (Caselli et al. 2010) imply values of $\sim 10^{-10}$.

Within the shock front the gas heats up, and some reactions with barriers and endothermic reactions occur. Also, the heating of electrons leads to enhanced electron impact rates on the grains, and the drift of the ions relative to the grains contributes further to efficient ion recombination on grains, reducing the fractional ionisation within the shock. As usual, the primary sequence for H_2O formation in the shock involves the reactions of O and OH with H_2 . Figure 1 shows the fractional abundance of water produced in the shock as a function of the shock speed. At the lowest shock speed (i.e. 5 km s^{-1}), the shocked gas does not reach high enough temperatures to cause the conversion of much oxygen to water. At a shock speed of 10 km s^{-1} a few percent of the gas phase oxygen is converted to water, but it is only at shock speeds close to 20 km s^{-1} and above at which the atomic oxygen abundance falls by several

orders of magnitude, and nearly all of the gas phase oxygen is in water. The H_2O abundance is then a few times 10^{-4} .

3.2 Mantle sputtering

Within a C-type shock, grains experience high-speed impacts with gas particles. Sputtering leads to a continuous erosion of the icy grain mantle by which water is returned to the gas phase.

Grain mantle sputtering occurs for impact speeds $> 10/\sqrt{\mu} \text{ km s}^{-1}$ with μ the mean mass of the impacting species in atomic mass units (e.g. May et al. 2000). Since CO is the most massive abundant projectile with $\mu = 28$, mantle sputtering starts for grain-neutral drift speeds as low as $\approx 2 \text{ km s}^{-1}$. (Note from Fig. 2 that appreciable sputtering only occurs at drift speeds above 6 km s^{-1}). This value of the drift speed is independent of the grain size, because the mantle molecules are bound with the same energy. However, the threshold drift speed is reached at different shock speeds for the small and large grains. Small grains have Hall parameters¹ that are large enough that they move with the ions and electrons. The Hall parameter for the large grains is above unity but

¹ The Hall parameter is the ratio between the gyrofrequency of a charged

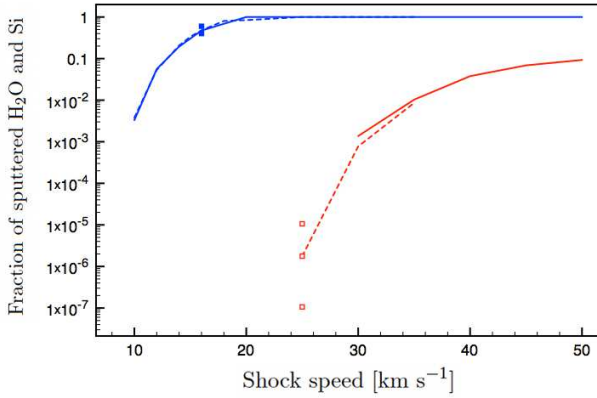


Figure 3. The fraction of mantle ice (blue) and core silicon (red) released in the gas-phase by sputtering as function of shock speed for values of n_{H0} of 10^4 cm^{-3} (solid) and 10^6 cm^{-3} (dashed). The squares show the sputtering fractions for shock angles of 30, 45 and 60 degrees for selected shock speeds; the sputtering efficiency decreases with increasing angle.

sufficiently small that they are only moderately coupled to the magnetic field and, thus, move at velocities between those of the electrons and the neutrals. Consequently, the grain-neutral drift speed for the large grains is smaller than for the small grains at a given shock speed.

No projectile induces noticeable sputtering when $v_s = 5 \text{ km s}^{-1}$, but when v_s has a higher value, small grains are sputtered. Table 2, as well as Fig. 3, displays the fraction of the initial mantle ice that is sputtered by a shock for which $\theta = 45^\circ$. Results are given for various values of the shock speed and values of n_{H0} of 10^4 cm^{-3} and 10^6 cm^{-3} . It also gives the enhancement in the downstream gas phase water fractional abundance due to sputtering. If we define the sputtering threshold shock speed as the shock speed for which 1% of the ice is removed (cf. Caselli et al. 1997), the threshold shock speed for small grain sputtering is 10 km s^{-1} and for large grain sputtering it is 10 (12) km s^{-1} for an upstream number density of 10^4 (10^6) cm^{-3} .

One also sees that the fraction of material sputtered from small grains is not very sensitive to n_{H0} , but particularly at lower shock speeds the fraction of material sputtered from the large grains does depend on n_{H0} . This again is a result of the coupling of the grains to the magnetic field (see above). The large grains have a larger Hall parameter in the lower density regime and, thus, have a larger neutral-grain drift speed than in the high-density regime.

For shocks for which $\theta = 45^\circ$, the highest sputtering rate per unit time per unit volume of mantles is due to collisions with CO for shock speeds less than about 10 km s^{-1} and to collisions with H_2O for speeds above about 14 km s^{-1} . At intermediate speeds, collisions with O also contribute non-negligibly as the relative importance of CO and H_2O collisions varies. Above 30 km s^{-1} , H_2 dominates the sputtering of both grain types. However, at these shock speeds, the icy mantles of both grain species are completely eroded. The contribution of the grain sputtering to the water abundance is even then negligible compared to the contribution of the gas-phase oxygen conversion (see Fig. 1).

particle and the collisional momentum transfer frequency of the charged particle with neutrals.

3.3 Core sputtering

Once the grain mantles are vapourised, the grain cores begin to erode as long as the impact speeds of the projectiles are high enough. As the binding energy of a particle in the grain core is higher than in the mantle, higher grain-neutral drift speeds are necessary. Again CO is the sputtering projectile of most importance at lower speeds, and small grains start to contribute to the SiO gas-phase abundance at shock speeds of 25 km s^{-1} (see Fig. 3 for shocks for which $\theta = 45^\circ$). This result is similar to the one of Caselli et al. (1997) and May et al. (2000). Collisions with CO dominate the sputtering at shock speeds up to 30 km s^{-1} . Above shock speeds of about 35 km s^{-1} the highest sputtering rate per unit time per unit volume of elemental silicon is due to collisions with H_2O . Table 3 displays the fraction of the initial core elemental silicon that is sputtered. It also gives the enhancement in the downstream gas phase SiO fractional abundance due to sputtering.

Similarly to the results for mantle sputtering, the core sputtering of the small grains is independent of n_{H0} (as their Hall parameter is much larger than unity). The large grains are more efficiently sputtered in the low-density regime but contribute only a negligible amount to the SiO gas-phase abundance. For a range of shock speeds, the SiO production rises with increasing speed with values similar as in Fig. 2 of Gusdorf et al. (2008a). However, the SiO abundance reaches an upper limit as C-type shocks do not exist for shock speeds above a certain value. For higher shock speeds, shocks are of J-type. For $n_{H0} = 10^4 \text{ cm}^{-3}$ the transition occurs for a shock speed between 50 and 55 km s^{-1} , while a J-type shock occurs for a minimum shock speed between 35 and 40 km s^{-1} for $n_{H0} = 10^6 \text{ cm}^{-3}$. At these speeds the grain cores are not completely destroyed, i.e. only a few percent of the core is removed in the high-density case and about a third of the core is destroyed in the low-density regime. Hence, the maximum SiO fractional abundance differs by an order of magnitude between the two density regimes.

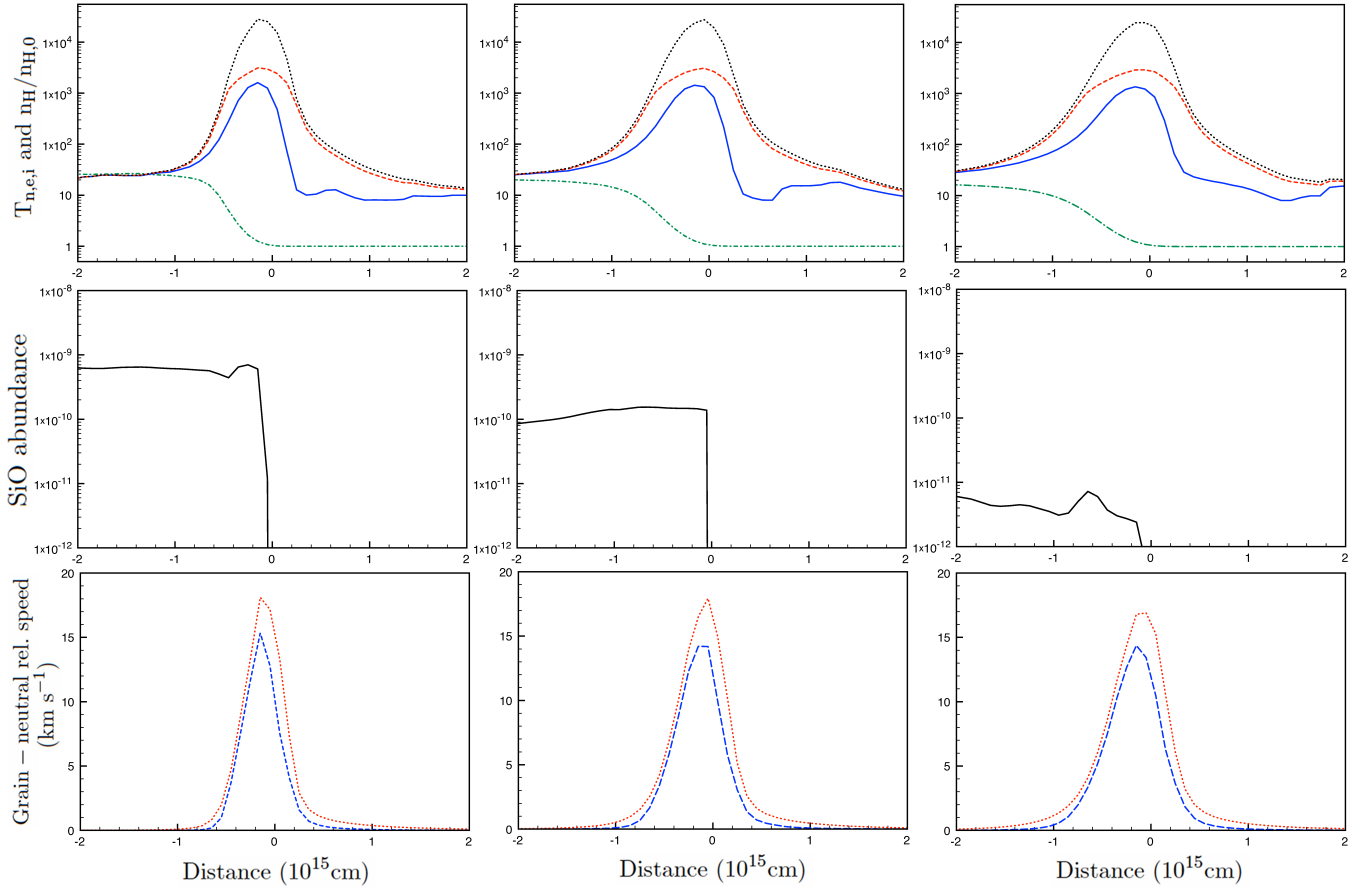
3.4 Angular dependence

Up to now we have discussed the grain sputtering for an oblique shock for which $\theta = 45^\circ$. However, Van Loo et al. (2009) showed that the shock properties, such as the shock width, change as function of θ . Therefore, variations, with angle, of the H_2O and SiO abundances due to sputtering is expected.

Figure 2 presents results for 16 km s^{-1} shocks propagating into media with $n_{H0} = 10^4 \text{ cm}^{-3}$ at angles of 30° , 45° and 60° with respect to the upstream magnetic field. The fraction of the ice that is sputtered from each type of grain, rather than the gas phase abundance of water, is shown because much of the gas phase water exists due to the conversion of upstream gas phase atomic oxygen to water. The results in Fig. 2 indicate that the H_2O abundance is lowest in the shock with the largest width. It is obvious that the shock width is irrelevant for the level of sputtering as the sputtering depends mainly on the neutral-grain drift speeds. As the bottom row of Fig. 2 shows, the peak small and large grain-neutral drift speeds are smallest at large angles; they are 10.5 km s^{-1} at 30° , 10 km s^{-1} at 45° and 9.5 km s^{-1} at 60° . This behaviour is consistent with the results shown in Fig. 2 of Van Loo et al. (2009) who found that the y and z components of the velocities of charged species are greater for smaller angles. Furthermore, the length scale over which the drift speeds are higher than 6 km s^{-1} , i.e. the minimum drift speed for which mantle sputtering is efficient, are similar for all angles. The angular variations in the fraction of water that

Table 3. Fraction of core elemental silicon that is sputtered and gas phase SiO fractional abundance enhancement due to sputtering. Results are given for large and small grains and for both combined.

Large grains				Small grains		Small & large grains	
Shock Speed (km s ⁻¹)	n _{H0} (cm ⁻³)	Fraction of Si removed	Contribution to downstream SiO	Fraction of Si removed	Contribution to downstream SiO	Fraction of Si removed	Contribution to downstream SiO
20	1.00(4)	0.00	-	<1.00(-4)	≈0.00	<1.00(-4)	≈0.00
30	1.00(4)	3.62(-4)	1.60(-8)	4.58(-3)	6.40(-8)	1.37(-3)	8.00(-8)
35	1.00(4)	2.83(-3)	1.25(-7)	3.40(-2)	4.75(-7)	1.03(-2)	6.00(-7)
40	1.00(4)	5.59(-3)	2.47(-7)	1.40(-1)	1.95(-6)	3.78(-2)	2.20(-6)
45	1.00(4)	1.12(-2)	4.94(-7)	2.51(-1)	3.51(-6)	6.87(-2)	4.00(-6)
50	1.00(4)	2.60(-2)	1.15(-6)	3.04(-1)	4.25(-6)	9.28(-2)	5.40(-6)
<hr/>							
20	1.00(6)	0.00	-	0.00	-	0.00	-
25	1.00(6)	0.00	-	7.37(-6)	1.03(-10)	1.77(-6)	1.03(-10)
30	1.00(6)	0.00	-	3.22(-3)	4.50(-8)	7.73(-4)	4.50(-8)
35	1.00(6)	9.76(-4)	4.31(-8)	3.26(-2)	4.56(-7)	8.57(-3)	4.99(-7)

**Figure 4.** Gas phase fractional abundance of SiO for a shock speed of 25 km s⁻¹, n_{H0} = 10⁶ cm⁻³ and θ of 30° (left column), 45° (middle column) and 60° (right column). The top row gives the ion (black, dotted), electron (red, dashed) and neutral (blue, solid) temperatures, as well as the neutral density normalised to its upstream value (green, dash-dotted). The middle row shows the gas phase fractional abundances of SiO. The bottom row displays the speed of small (red, dotted) and large (blue, dashed) grains relative to neutrals in km s⁻¹.

is sputtered are significant and range from 0.4 at 60° to 0.6 at 30° . Such variations disappear with increasing shock speed because for high enough speeds vaporisation of the grain mantle is complete for all angles.

Figure 4 presents results for 25 km s^{-1} shocks propagating into media with $n_{\text{H}0} = 10^6 \text{ cm}^{-3}$ at angles of 30° , 45° and 60° with respect to the upstream medium. The results in Fig. 4 show that the SiO abundance too is lowest in the shock with the largest width. Again these differences can be attributed to the peak small grain-neutral drift speeds which are smallest at large angles; they are 18.2 km s^{-1} at 30° , 18 km s^{-1} at 45° and 17 km s^{-1} at 60° . Contrary to the H_2O results, these modest differences in drift speeds have large effects on the amount of elemental silicon that is sputtered, i.e. there is a difference of two orders of magnitude between the SiO abundance at 30° and 60° . However, note that the shock speed is close to the threshold speed for core sputtering. Then small variations in the drift speed can mean the difference between core sputtering or no sputtering at all. For higher shock speeds the angular differences in SiO abundance are less pronounced, but the trend of lower abundances for larger θ remains.

4 DISCUSSION AND CONCLUSIONS

In this paper we present the first self-consistent multifluid MHD simulations of grain mantle and core sputtering in oblique C-type shocks propagating through dusty media. The small grains are more tightly coupled to the magnetic field than the large grains with a strong coupling in both low- and high-density regimes. This maximises the drift speeds between the small grains and the neutral sputtering projectiles resulting in more efficient sputtering of the small grains. Mantle sputtering starts at shock speeds of about 10 km s^{-1} , and the mantles are completely vapourised for shock speeds around $20\text{--}25 \text{ km s}^{-1}$. The sputtering of the icy mantles returns water back to the gas phase. However, neutral-neutral chemistry dominates the production of gas phase water by an order of magnitude.

Once the mantles are completely eroded, core sputtering commences and releases silicon to form SiO. The abundance of SiO in the gas phase never saturates as even at the critical speed for the transition from C- to J-type shocks not all of a grain core is destroyed. While the critical speed is $50\text{--}55 \text{ km s}^{-1}$ for $n_{\text{H}0} = 10^4 \text{ cm}^{-3}$, it is only 40 km s^{-1} for $n_{\text{H}0} = 10^6 \text{ cm}^{-3}$. For a given shock speed the efficiency of small grain sputtering is not sensitive to the density. Consequently, the density dependence of the C- to J-type transition means that higher SiO abundances can be produced by shocks in the low-density regime.

An important result is that the sputtering yields depend on the angle between the magnetic field and the shock normal. Especially, at the threshold drift speeds for mantle or core sputtering, small angular variations can induce large changes in abundances. For example, for shocks propagating at 25 km s^{-1} in media with number densities of 10^6 cm^{-3} , the SiO abundance differs by two orders of magnitude for $\theta = 30^\circ$ and 60° . This has important consequences for the interpretation of observations. For example, discrete emission features in SiO observations have been ascribed to different shocks being present within the telescope beam (e.g. Jiménez-Serra et al. 2009). However, such features can be explained by a bow shock interacting with an inhomogeneity in the medium. The flanks of the bow shock have lower speeds than the head and also make different angles with the magnetic field. In an inhomogeneous medium some regions of the bow-shock are then

highlighted resulting in discrete SiO emission features. Such an assumption, however, needs to be further examined by extending the planar shock model to multiple dimensions.

Direct comparisons of the results with those of other researchers is complicated as the only previous work (Caselli et al. 1997) on sputtering in oblique shocks is not based on self-consistent shock models. Also, the treatment of core sputtering in that work differed from that developed by May et al. (2000) and used in subsequent work. However, the results given in Table 3 for the fraction of elemental silicon sputtered from small grains are in harmony with the results of Caselli et al. (1997) for a shock for which $\theta = 45^\circ$. Other self-consistent studies concern only perpendicular shocks ($\theta = 90^\circ$) and, thus, should find similar, although lower, values for shock speed exceeding the threshold value for sputtering. Gusdorf et al. (2008a), who assumed a somewhat larger upstream magnetic field strength and different grain population, found that the fraction of silicon that is sputtered is about 0.04 for $n_{\text{H}0} = 10^4 \text{ cm}^{-3}$ and a shock speed 40 km s^{-1} . Guillet et al. (2011) who adopt a kinetic method for the dust grain dynamics in favour of a fluid approach, find a value of 0.02 for the same model as Gusdorf et al. (2008a). The corresponding result given in Table 3 is 0.04.

The SiO abundances found in our simulations only represent upper limits. Observations indicate that silicate-based grains only account for about 75% of the interstellar dust mass with the rest of the mass stored in carbonaceous grains or PAHs (Draine 2011). Furthermore, the conversion of atomic silicon into SiO is not fully efficient above densities of 10^5 cm^{-3} which possibly reduces the SiO abundance due to sputtering by an order of magnitude (Gusdorf et al. 2008b).

Unlike Gusdorf et al. (2008a) and Guillet et al. (2011), who included grains 40 times smaller than the smallest that we have assumed to be present, we have not considered the destruction of grain material due to grain-grain collisions. Our choice to focus solely on sputtering first was based in part on a desire to understand the effects of obliqueness on sputtering before looking at the complicated way in which obliqueness, sputtering and grain-grain collisions all act together to destroy grains. Our decision to do so was informed by the estimates of Caselli et al. (1997) that showed for grain populations of the sizes that we selected, grain-grain collisions would contribute significantly to mantle removal only at shock speeds near the threshold even for high pre-shock densities. Our choice has allowed us to see that obliqueness affects sputtering near the threshold shock speed significantly. However, considering the findings of both Caselli et al. (1997) and of Guillet et al. (2011) for the return of silicon to the gas phase, as well as the results given in Figure 4, we conclude that the future inclusion of both grain-grain collisions and obliqueness in shock models is necessary to infer the threshold shock speed for the injection of significant quantities of silicon into the gas phase.

ACKNOWLEDGMENTS

We thank the anonymous referee for his/her constructive comments. The authors are grateful for the support provided by a studentship and successive rolling grants awarded by the UK Science and Technology Funding Council and from the SMA Postdoctoral Fellowship of the Smithsonian Astrophysical Observatory held by SVL.

APPENDIX A: PARTICLE CURRENT ONTO A GRAIN

Havnes et al. (1987) derived general expressions for the current of charged particles (with charge Z_j) onto a dust grain carrying a charge of Z_g .

For $Z_g Z_j \leq 0$,

$$\Gamma_{jg} = \pi a^2 n_j Z_j e \frac{c_j^2}{2v_{jg}} \left\{ \left(1 + 2 \left(\frac{v_{jg}}{c_j} \right)^2 - 2Z_j Z_g \xi \right) \times \operatorname{erf} \left(\frac{v_{jg}}{c_j} \right) + \frac{2(v_{jg}/c_j)}{\sqrt{\pi}} \exp \left(- \left(\frac{v_{jg}}{c_j} \right)^2 \right) \right\},$$

and, for $Z_g Z_j \geq 0$,

$$\Gamma_{jg} = \pi a^2 n_j Z_j e \frac{c_j^2}{2v_{jg}} \left\{ \frac{1}{2} \left(1 + 2 \left(\frac{v_{jg}}{c_j} \right)^2 - 2Z_j Z_g \xi \right) \times \left[\operatorname{erf} \left(\frac{v_{jg}}{c_j} + \sqrt{Z_j Z_g \xi} \right) + \operatorname{erf} \left(\frac{v_{jg}}{c_j} - \sqrt{Z_j Z_g \xi} \right) \right] + \frac{1}{\sqrt{\pi}} \left(\frac{v_{jg}}{c_j} + \sqrt{Z_j Z_g \xi} \right) \exp \left(- \left(\frac{v_{jg}}{c_j} - \sqrt{Z_j Z_g \xi} \right)^2 \right) + \frac{1}{\sqrt{\pi}} \left(\frac{v_{jg}}{c_j} - \sqrt{Z_j Z_g \xi} \right) \exp \left(- \left(\frac{v_{jg}}{c_j} + \sqrt{Z_j Z_g \xi} \right)^2 \right) \right\},$$

where a is the grain radius, n_j the number density of the charged fluid, v_{jg} the relative drift velocity between the grain and the charged fluid, c_j the sound speed of the charged fluid and $\xi = e^2 / ak_B T$. The charged fluid can be the ion or electron fluid.

REFERENCES

- Anders E., Grevesse N., 1989, *GeCoA*, 53, 197
 Ashmore, I., van Loo, S., Caselli, P., Falle, S. A. E. G., & Hartquist, T. W. 2010, *A&A*, 511, A41
 Bergin, E. A., et al. 2000, *ApJL*, 539, L129
 Bergin, E. A., & Snell, R. L. 2002, *ApJL*, 581, L105
 Caselli, P., Hartquist, T. W., & Havnes, O. 1997, *A&A*, 322, 296
 Caselli, P., Keto, E., Pagani, L., et al. 2010, *A&A*, 521, L29
 Chapman J. F., Wardle M., 2006, *MNRAS*, 371, 513
 Draine, B. T., & Salpeter, E. E. 1979, *ApJ*, 231, 77
 Draine, B. T., Roberge, W. G., & Dalgarno, A. 1983, *ApJ*, 264, 485
 Draine, B. T. 2011, *EAS Publications Series*, 46, 29
 Falle, S. A. E. G. 2003, *MNRAS*, 344, 1210
 Flower, D. R., & Pineau des Forêts, G. 1995, *MNRAS*, 275, 1049
 Flower, D. R., Pineau des Forêts, G., & Hartquist, T. W. 1985, *MNRAS*, 216, 775
 Guillet V., Pineau des Forêts G., Jones A. P., 2007, *A&A*, 476, 263
 Guillet, V., Jones, A. P., & Pineau des Forêts, G. 2009, *A&A*, 497, 145
 Guillet, V., Pineau des Forêts, G., & Jones, A. P. 2011, *A&A*, 527, A123
 Gusdorf A., Cabrit S., Flower D. R., Pineau Des Forêts G., 2008a, *A&A*, 482, 809
 Gusdorf, A., Pineau des Forêts, G., Cabrit, S., & Flower, D. R. 2008b, *A&A*, 490, 695
 Hartquist, T. W., Dalgarno, A., & Oppenheimer, M. 1980, *ApJ*, 236, 182
 Havnes, O., Hartquist, T. W., & Pilipp, W. 1987, *NATO ASIC Proc. 210: Physical Processes in Interstellar Clouds*, 389

- Hollenbach, D., & McKee, C. F. 1979, *ApJS*, 41, 555
 Jiménez-Serra, I., Caselli, P., Martín-Pintado, J., & Hartquist, T. W. 2008, *A&A*, 482, 549
 Jiménez-Serra, I., Martín-Pintado, J., Caselli, P., Viti, S., & Rodríguez-Franco, A. 2009, *ApJ*, 695, 149
 Mathis, J. S., Rumpl, W., & Nordsieck, K. H. 1977, *ApJ*, 217, 425
 May, P. W., Pineau des Forêts, G., Flower, D. R., Field, D., Allan, N. L., & Purton, J. A. 2000, *MNRAS*, 318, 809
 Meyer D. M., Jura M., Cardelli J. A., 1998, *ApJ*, 493, 222
 Millar, T. J., Farquhar, P. R. A., & Willacy, K. 1997, *A&AS*, 121, 139
 Neufeld, D. A., & Melnick, G. J. 1987, *ApJ*, 322, 266
 Neufeld, D. A., Lepp, S., & Melnick, G. J. 1995, *ApJS*, 100, 132
 Pilipp, W., & Hartquist, T. W. 1994, *MNRAS*, 267, 801
 Pilipp, W., Hartquist, T. W., & Havnes, O. 1990, *MNRAS*, 243, 685
 Snow T. P., & Witt A. N., 1996, *ApJ*, 468, L65
 Schilke, P., Walmsley, C. M., Pineau des Forêts, G., & Flower, D. R. 1997, *A&A*, 321, 293
 Van Loo, S., Ashmore, I., Caselli, P., Falle, S. A. E. G., & Hartquist, T. W. 2009, *MNRAS*, 395, 319
 Wardle, M. 1998, *MNRAS*, 298, 507
 Whittet, D. C. B., & Duley, W. W. 1991, *A&A Rev.*, 2, 167
 Woodall, J., Agúndez, M., Markwick-Kemper, A. J., & Millar, T. J. 2007, *A&A*, 466, 1197